Supporting Information for Halide perovskite artificial solids as a new platform to simulate collective phenomena in doped Mott insulators

Alessandra Milloch,[1,2,3,*] Umberto Filippi,[4] Paolo Franceschini,[5,6] Michele Galvani,[1] Selene Mor,[1,2] Stefania Pagliara,[1,2] Gabriele Ferrini,[1,2] Francesco Banfi,[7] Massimo Capone,[8] Dmitry Baranov,[4,9] Liberato Manna,[4] and Claudio Giannetti[1,2,5,†]

[1] *Department of Mathematics and Physics, Università Cattolica del Sacro Cuore, Brescia I-25133, Italy*
[2] *ILAMP (Interdisciplinary Laboratories for Advanced Materials Physics), Università Cattolica del Sacro Cuore, Brescia I-25133, Italy*
[3] *Department of Physics and Astronomy, KU Leuven, B-3001 Leuven, Belgium*
[4] *Italian Institute of Technology (IIT), Genova 16163, Italy*
[5] *CNR-INO (National Institute of Optics), via Branze 45, 25123 Brescia, Italy*
[6] *Department of Information Engineering, University of Brescia, Brescia I-25123, Italy*
[7] *FemtoNanoOptics group, Université de Lyon, CNRS, Université Claude Bernard Lyon 1, Institut Lumière Matière, F-69622 Villeurbanne, France*
[8] *International School for Advanced Studies (SISSA), via Bonomea 265, Trieste*
[9] *Division of Chemical Physics, Department of Chemistry, Lund University, P.O. Box 124, SE-221 00 Lund, Sweden*

S1. MAPPING OF THE EXCITONIC MOTT TRANSITION

The mapping between the Hamiltonian describing the exciton-gas → electron-hole-liquid transition in photoexcited semiconductors and the repulsive Hubbard model ($\hat{H}_U$) in a magnetic field can be directly argued starting from the Hamiltonian describing an ensemble of symmetric spinless holes (created by $h^\dagger_{\mathbf{k}}$) and electrons (created by $e^\dagger_{\mathbf{k}}$) at momentum $\mathbf{k}$, with energy $\epsilon_{\mathbf{k}}$ and subject to a short-range electron-hole Coulomb attraction $-U$:

$$\hat{H}_{loc} = \sum_{\mathbf{k}} \epsilon_{\mathbf{k}} (h^\dagger_{\mathbf{k}} h_{\mathbf{k}} + e^\dagger_{\mathbf{k}} e_{\mathbf{k}}) - U \sum_i n_{ei} n_{hi} - \mu \sum_i (n_{ei} + n_{hi}) \tag{S1}$$

where the short-range Coulomb attraction -U is considered as momentum independent, $n_{e(h)i}$ represents the density of electrons(holes) at site i and μ is the chemical potential, which fixes the number of excited electron-hole pairs $n_{\rm eh}$=$\langle n_{ei}\rangle$=$\langle n_{hi}\rangle$.

By applying the transformations $e_i \rightarrow c_{i\downarrow}$ and $h_i \rightarrow (-1)^i c^\dagger_{i\uparrow}$, the Hamiltonian (S1) can be mapped into the Hamiltonian [1]:

$$\hat{H}_{loc} = \hat{H}_U - h \sum_i (n_{i\uparrow} - n_{i\downarrow}) \tag{S2}$$

where:

$$\hat{H}_U = -t \sum_{\langle ij\rangle \sigma} (c^\dagger_{i\sigma} c_{j\sigma} + c^\dagger_{j\sigma} c_{i\sigma}) + U \sum_i n_{i\uparrow} n_{i\downarrow} \tag{S3}$$

t being the hopping parameter, $n_{i\sigma}$ is the occupation number at site i of electrons with spin ↑ and ↓; $c^\dagger_{i\sigma}$ and $c_{i\sigma}$ are creation and annihilation operators for an electron of spin σ at site i.

* alessandra.milloch@unicatt.it
† claudio.giannetti@unicatt.it

S2. SAMPLE PREPARATION

A. Synthesis of cesium oleate stock solution

The cesium oleate stock solution was prepared by loading 0.4 g of cesium carbonate (Cs_2CO_3, 99%), 1.75 ml of oleic acid (OA, 90%) and 15 ml octadecene-1 (ODE, 90%) into a 40 ml vial and placing it into an aluminum block preheated at 120 °C on top of a hotplate. The mixture was stirred under N_2 flow and its temperature was kept between ∼110-115 °C until all visible solid disappeared (∼60 minutes). The mixture was eventually cooled down on a room temperature hotplate under stirring.

B. Synthesis of $CsPbBr_3$ nanocubes

$CsPbBr_3$ nanocubes (NCs) were synthesized following the method reported in Ref. 2 and Ref. 3 with minor variations. In a 20 ml vial, 72 mg of lead (II) bromide ($PbBr_2$, $\geqslant$ 98%) were combined with 5 ml of ODE, 0.5 ml of oleylamine (OLAm, 70%) and 0.05 ml of OA. The vial was equipped with a magnetic stirrer and placed into an aluminum block preheated at 185 °C on top of a hotplate. As the temperature of the mixture reached 170 °C, the vial was lifted from the block and fixed with a clamp above the hotplate and as soon as it cooled down to 160 °C, 0.5 ml of the cesium oleate stock solution were swiftly injected. The reaction was quenched after ∼ 7 seconds with a cold water bath (∼ 20 °C) under stirring. The crude solution was centrifuged for 3 minutes at 4000 rpm and the supernatant was discarded. Then the solution was centrifuged again at 4000 rpm for 3 minutes to discard any remaining liquid, with the vials in the centrifuge oriented such that the precipitate was pointing outwards. The remaining liquid was removed with a 100 µl mechanical micropipette, and the step was repeated again, this time using a cotton swab to collect the liquid. The remaining solid was dissolved in 1 ml of toluene (99.7%) and filtered through 0.45 µm hydrophobic PTFE syringe filter to eliminate any residual aggregates.
The solution for photoluminescence (PL) and absorbance measurements was prepared by diluting 6 µl of the NC solution in a 2994 µl of toluene in a quartz cuvette. NC batches were considered suitable for self-assembly experiments when the full width at half maximum (FWHM) of the PL spectrum was $<$ 90 meV. Absorbance was measured through 10 mm path length, and the NC concentration was calculated from Beer's law by using absorbance at 335 nm and a published size-dependent extinction coefficient [4]. Typical concentration varied in the range of ∼ 4-4.5 µM.

C. Preparation of $CsPbBr_3$ nanocubes superlattice and disordered film

Self-assembly of $CsPbBr_3$ NCs was carried out using a slow solvent evaporation method on 1 cm × 1 cm monocrystalline silicon (Si) and glass substrates (Figure S1a). The substrates were cleaned by rinsing with methanol and 2-propanol and dried by gentle tapping with an absorbing paper tissue and by blowing compressed air.
Three substrates were placed inside a Petri dish and 30 µl of the stock solution of $CsPbBr_3$ NCs in toluene were drop-casted on each of them. The solvent was allowed to slowly evaporate (∼12 hours), after which films were considered ready to be used for experiments.
The disordered films of $CsPbBr_3$ NCs were instead prepared by collecting the precipitate of the crude solution after the three centrifugation steps and by mechanically scrambling and pressing it with a plastic scoop and eventually spreading it on 0.5 cm × 1 cm Si or glass substrates (Figure S1b).
Samples thickness was measured from scanning electron microscopy (SEM) images of middle film profiles obtained by breaking in half replicas of samples used for experiments. Estimated sample thickness for the SL films was 7 µm $\leqslant$ $thickness_{SL}$ $\leqslant$ 15 µm, and for the disordered films was 10 µm $\leqslant$ $thickness_{dis}$ $\leqslant$ 20 µm.

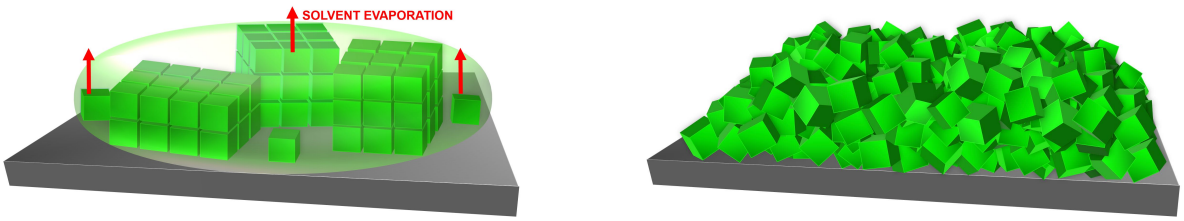

(a) (b)

FIG. S1: (a) Schematic representation of SLs formation during slow solvent evaporation and of (b) randomly oriented NCs on a silicon substrate.

S3. CHARACTERIZATION OF SL AND DISORDERED FILMS

A. Photoluminescence and absorbance

The samples were optically characterized by absorption and photoluminescence (PL) spectra, acquired with a Cary 300 spectrophotometer and with a Cary Eclipse spectrofluorometer, respectively. The equilibrium PL and absorption spectra of NCs dispersed in toluene and of NC deposited on a glass substrate are displayed in Figure S2a and b for disordered NC and superlattices respectively. In both cases, we observe a PL red-shift (ΔPL_{NC} = 2.414 eV - 2.382 eV = 32 meV for the disordered NCs sample and ΔPL_{SL} = 2.414 eV - 2.386 eV = 28 meV for the SLs sample) and a PL peak broadening ($\Delta FWHM_{NC}$ = 142 meV − 86 meV = 55 meV for disordered NCs and $\Delta FWHM_{SL}$ = 116 meV - 86 meV = 30 meV for SLs) for the deposited films compared to NCs in toluene dispersion, consistently with previous observations [2, 5–8].

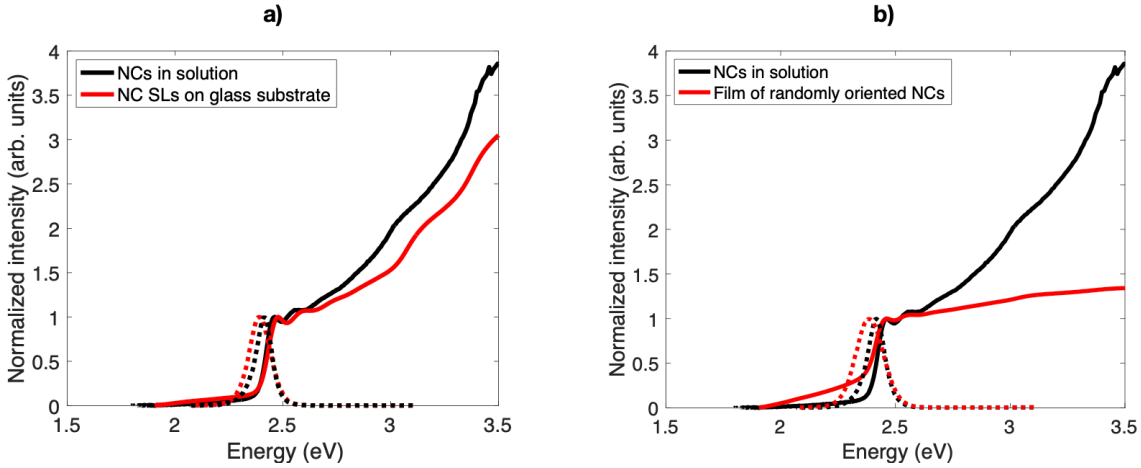

FIG. S2: a) Room temperature PL (dashed line) and absorption (solid line) spectra of NCs dispersed in toluene (black) and of disordered NCs on a glass substrate (red). b) Room temperature PL (dashed line) and absorption (solid line) spectra of NCs dispersed in toluene and of NC SLs deposited on a glass substrate.

B. X-ray diffraction

X-ray diffraction (XRD) patterns collected from disordered NCs film and superlattice sample are shown in Figure S3. The XRD data were measured with a PANalytical Empyrean diffractometer in a parallel beam configuration, equipped with a Cu Kα (λ = 1.5406 Å) ceramic X-ray tube operating at 45 kV and 40 mA, 1 mm wide incident and receiving slits, and a 40 mA PIXcel3D 2×2 two-dimensional detector.
For disordered NCs, the XRD pattern shows the Bragg reflections ascribed to the orthorhombic structure of $CsPbBr_3$ [9] and all the peaks expected from a film of randomly oriented NCs [3]. Conversely, for the SL sample, we observe the presence of two strong peaks at $2\theta \sim 15°$ and $2\theta \sim 30.5°$. As described in detail in previous works [3, 10], this XRD pattern originates from a close-packing of the cubes in the plane parallel to the substrate, which leads to the enhanced Bragg reflections from (110), (1$\bar{1}$0) and (002) ($2\theta \sim 15°$) and (220), (2$\bar{2}$0) and (004) ($2\theta \sim 30.5°$) planes of the orthorombic unit cell of $CsPbBr_3$. The precise periodicity between NCs inside SLs produces a phase modulation on the diffracted X-rays, causing additional interference which produces the fine structure for the $2\theta \sim 15°$ peak, observable in Figure S3b (black solid line).

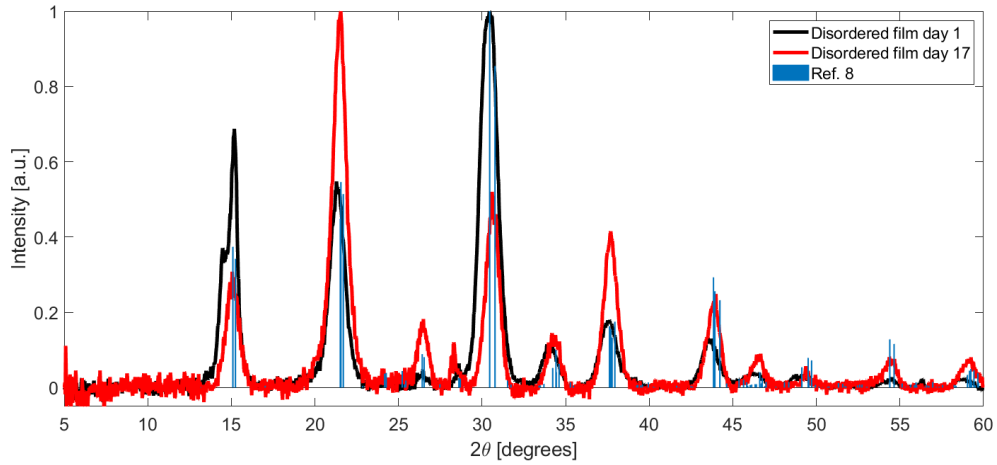

(a)

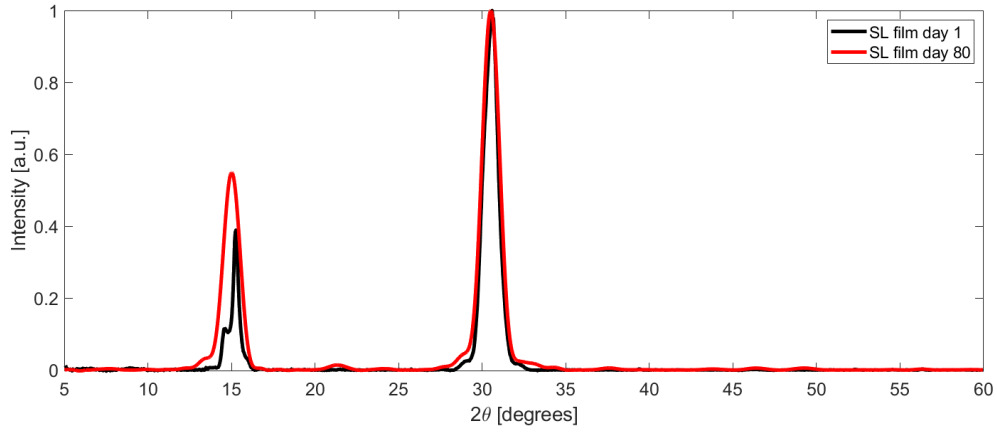

(b)

FIG. S3: XRD patterns of disordered NCs film (a) and superlattice film (b). The blue lines in (a) represent the Bragg peaks positions reported in literature (ref. 9) for $CsPbBr_3$.

C. Optical microscopy

Optical microscope images of the NCs films, acquired on a ZETA-20 true color 3D optical profiler, are displayed in Figure S4. For the disordered NCs film (Fig. S4a), the image shows a roughly homogeneous spatial distribution of $CsPbBr_3$ NCs; no well-defined micron-sized rectangular structure, that typically corresponds to SLs, is observable in the sample, suggesting that mechanical scrambling produces largely disordered NC film. In the SL sample (Fig. S4b), the NCs are assembled into aggregates of rectangular shape and size between 1 and 10 µm, each corresponding to a NC superlattice.

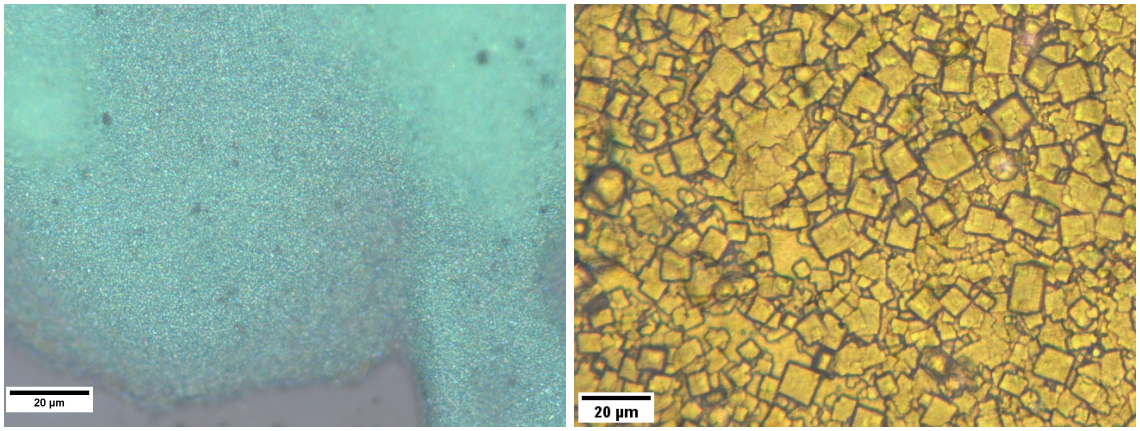

(a) (b)

FIG. S4: Optical microscopy images of disordered NCs film (a) and superlattice film (b).

S4. SAMPLE AGING

Pump-probe experiments were performed on samples with various ages, from fresh ($\sim$ day 4) to $\sim$ 90 days old ones. The data presented in the main text were acquired on 30-35 days old disordered NCs sample and 85-92 days old SL sample. When not used for experiments the films were stored in a vacuum desiccator cabinet at $\sim$1 mbar. Aging effects are investigated by means of XRD and optical microscopy.

A. Disordered NCs film

Figure S3a shows the XRD pattern of the fresh (day 1, black solid line) and aged (day 17, red solid line) disordered film. The latter measurement was done after the film had been mounted in the cryostat employed for pump-probe experiments and had been subjected to ambient pressure-to-vacuum cycles and to room temperature-to-17 K cycles. As observable, both XRD patterns show, with different ratios in the peak intensities, the Bragg reflections ascribed to the orthorhombic structure of $CsPbBr_3$, as expected for a film of disordered NCs. Nevertheless, for the day 1 measurement, the peak at $2\theta \sim 15°$ shows a splitting, which suggests that when the film was deposited, NCs assembled and arranged in a periodic way in some form of super-structures. The size of these superstructures must be $\leqslant$ 1 µm, since they are not observable with optical microscopy (Figure S4a) and neither with SEM, where just a rough surface is noticeable. After 17 days and after being subjected to several vacuum and temperature cycles, the splitting at the $2\theta \sim 15°$ peak disappears, suggesting that the periodic arrangement is lost. Since all the pump and probe measurements on disordered film were conducted after this last XRD measurement, we can assume that the disordered film we measured is made of randomly oriented and randomly packed NCs.

B. SL film

Figure S3b shows XRD patterns of fresh (day 1, black solid line) and aged (day 80, red solid film) films of densely packed $CsPbBr_3$ NC SLs. The XRD pattern of the fresh SL film was collected immediately after the evaporation of the solvent ($\approx$ 12 hours after dropcasting solution on Si substrate), while the XRD pattern of the aged SL film was collected after pump and probe experiments, i.e. after the sample had undergone several cycles of vacuum and of cryogenic temperatures. We observe that, also in the aged sample, the main diffraction contribution comes from two peaks ($2\theta \sim 15°$ and $2\theta \sim 30°$), but the fine structure for the $2\theta \sim 15°$ peak is lost upon aging. This superlattice interference is closely related to the statistical fluctuation of the NC spacing, indicated by σ_l. It represents the stacking disorder of NCs and its effect on the diffraction profile is to smear fringes, making them disappear when its value becomes too high, leaving just one peak profile dependent on atomic plane periodicity and NC thickness.

Table I and Figure S5 summarize the results obtained by fitting the XRD pattern of the fresh and aged films, by means of the multilayer diffraction method described in Ref. 10. After 90 days, an increase of σ_l from 1.321 Å to 2.322 Å (relative increase of $\sim$ 75%) is observed. This is consistent with the XRD pattern of the aged film shown in Figure S3b, which displays no fringes at the $2\theta \sim 15°$ peak. A decrease of the interparticle spacing l is also observed after 90 days, from 34.2 Å to 29.4 Å. This is attributed to the removal of entrapped solvent (toluene) molecules during the application of vacuum: if we consider the volume of toluene molecule, which is equal to $\sim$177 $Å^3$, and we approximate the volume to the one of a cube, we get an edge equal to $\sim$5.6 Å. That value is comparable to the contraction of l from fresh to aged sample (4.8 Å) obtained from the fit. It is noteworthy that the average number of atomic planes per NC, N, does not change according to the fit. That implies NCs do not undergo a significant coarsening. Control experiments (not shown) were performed to verify that after applying vacuum the only change in the results of XRD pattern fitting is the decrease of interparticle spacing l due to solvent removal and, subsequently, to verify that upon cooling the sample (to 84 K in this case) no change in l and σ_l was observed once the sample was returned to room temperature. These considerations allow us to claim that aging of these samples does not lead to aggregation or side reactions that could form other products [11]. The only aging effect appears to be the increase in disorder manifested as an increase in the inter-NC spacing fluctuation (as depicted in Figure S6), due to NC and ligand rearrangement. Nevertheless, despite the increased disorder, the aged film is still made of close-packed monodispersed NCs lying in planes parallel to the substrate. This is also confirmed by the images of the aged film obtained from optical microscopy and SEM (performed on a JEOL JSM-6490LA scanning electron microscope), displayed in Figure S7a and b respectively, where the clear rectangular shapes typical of $CsPbBr_3$ superlattices are observed. Size and density distribution of superlattice cubes show great variability on different regions of the sample both in the fresh samples and aged ones; no clear change can be appreciated with sample age in this regard, indicating that the morphology of aged samples remains similar to fresh one.

TABLE I: **Fitting parameter of multilayer diffraction model.** Results of XRD pattern fitting of fresh and aged films shown in Figure S5.

Parameter	Definition	Day 1	Day 80
d [Å]	Lattice constant	5.830	5.829
l [Å]	Interparticle spacing	34.186	29.384
σ_l [Å]	Interparticle spacing fluctuation	1.321	2.322
N [atomic planes]	Number of atomic planes for NC	14.394	14.306
σ_N [atomic planes]	Size distribution of NCs	1.760	2.150
q-zero correction [Å]	Correction of diffractometer misalignment	0.004	0.012
NC edge [nm]	(N-1)×d	7.8 ± 0.3	7.7 ± 0.4

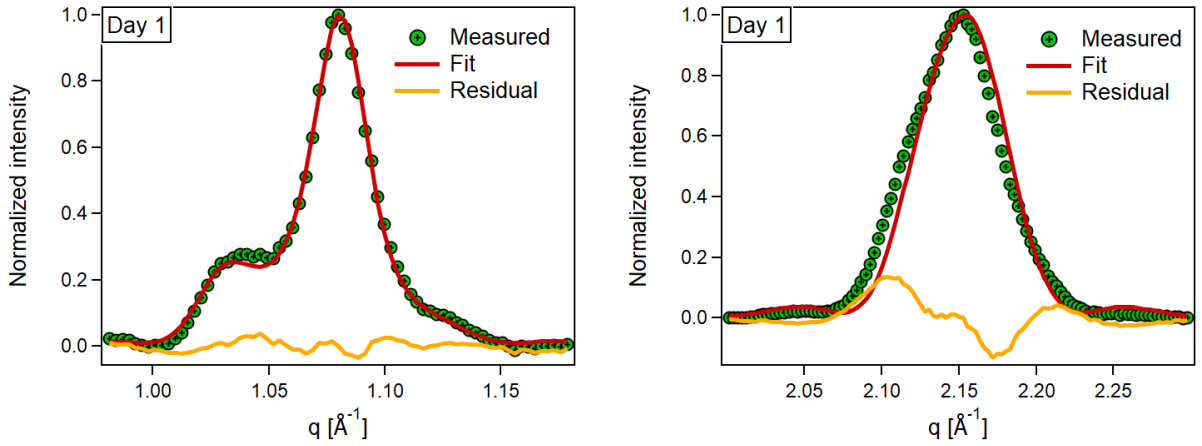

(a)

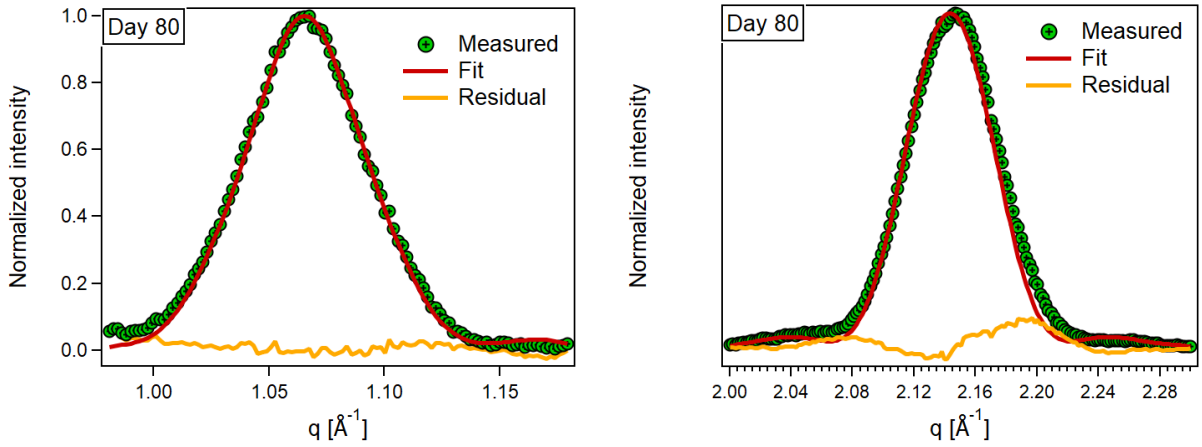

(b)

FIG. S5: Fitting of $2\theta \sim 15°$ and $2\theta \sim 30.5°$ (q $\sim$ 1.065, 2.111 Å^{-1} respectively, q $= (4\pi/\lambda_{exc})\sin(\theta)$) XRD peaks of fresh (a) and aged (b) films performed by means of the multilayer diffraction model described in Ref. 10.

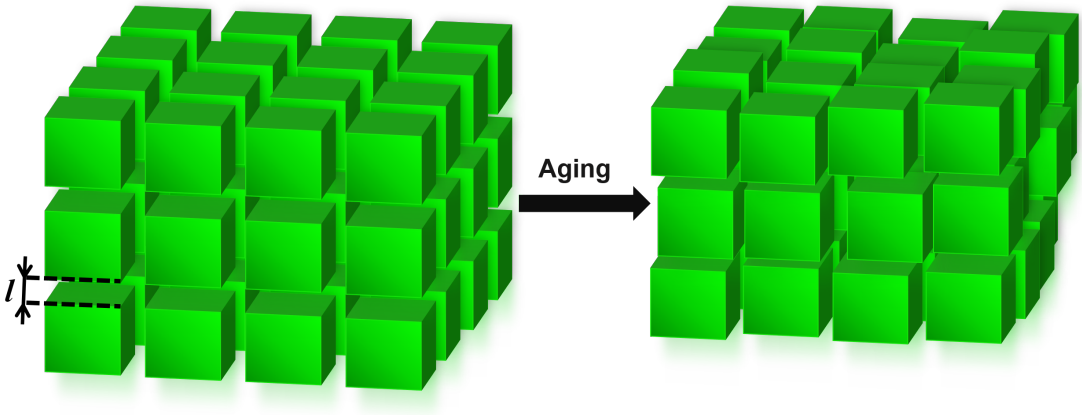

FIG. S6: Cartoon of the main effect of aging that causes a decrease of NC spacing in SLs and an increase of NC spacing fluctuations. The NC close packing arrangement and preferential orientation is nevertheless preserved.

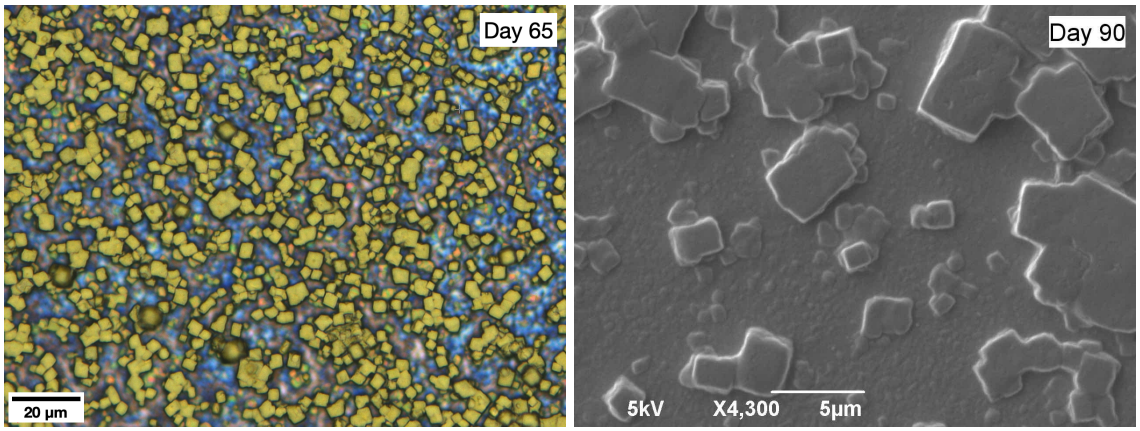

(a) (b)

FIG. S7: Optical microscope (a) and SEM (b) images of an aged SL film.

S5. PUMP-PROBE SPECTROSCOPY SETUP

The out of equilibrium properties of $CsPbBr_3$ superlattices and disordered NCs samples are investigated by means of broadband transient reflectivity experiments. The excitation is a 250 fs laser pulse at 2.41 eV photon energy (resonant with the excitonic level of the perovskite compound) and it is obtained by frequency doubling the emission of the laser system (Pharos by Light Conversion) in a 1-mm-thick BBO crystal. The induced variations in reflectivity are probed with a supercontinuum pulse, produced by means of White Light Generation process in a 4-mm-thick sapphire crystal pumped by a 1.6 eV photon energy pulse. The time delay between the arrival times of pump and probe pulses is controlled through a linearly motorized stage which delays the pump pulse in a time window covering $\sim$ 300 ps. The pump beam is focused to a 200 µm $\times$ 300 µm spot size, being $\approx$ 10 times larger than the probe spot size at the sample position (23 µm $\times$ 23 µm). The excitation intensity can be continuously varied between 0 and 400 $\mu J/cm^2$ by rotating a half-waveplate positioned on the pump beam path and followed by a polarizer that transmits the horizontally polarized component of the light. The probe beam is vertically polarized in order to allow filtering of the signal background, which is mainly given by sample scattering of the pump beam. The laser repetition rate employed in the measurements presented here is 400 kHz; no change in the sample response is observed upon decreasing the repetition rate while keeping fixed the energy per pulse of pump and probe beams. The signal detection is performed by lock-in acquisition of the reflected probe interferogram (generated by GEMINI interferometer, NIREOS) and computation of its Fourier transform at each fixed pump-probe time domain [12]. For pump-probe measurements, the samples are mounted inside a closed-cycle helium cryostat that allows to perform the ultrafast optical spectroscopy experiments at temperatures between 17 K and 300 K.

S6. EQUILIBRIUM OPTICAL PROPERTIES

Analysis of the pump-probe data by means of differential fitting of $\Delta R/R$ spectra requires a parametrization of the $CsPbBr_3$ optical constants at low temperature (T). We therefore build the real and imaginary parts of the low-T refractive index by employing a suitable Kramers-Krönig consistent model, where the relevant parameters are chosen in agreement with the energy values obtained from the experimental absorbance measured at room temperature (Fig. S2b) and with the temperature dependent trends reported in literature.

The real part of the optical conductivity, σ_1, is obtained as the sum of a sigmoid function, accounting for the conduction band edge, a Drude-Lorentz oscillator, describing the exciton resonance, and a background component modelled through a high-energy Drude-Lorentz oscillator (Figure S8a). The conduction band gap energy is red-shifted by $\sim$80 meV as compared to room temperature (Fig. S2b) and the amplitude of the exciton peak is increased compared to the edge amplitude, consistently with the temperature dependence of $CsPbBr_3$ absorption spectra reported in literature [13, 14]. The exciton binding is fixed at 43 meV, in agreement with literature reports [15, 16] and experimental absorbance (Fig. S2b). The imaginary part σ_2 is then computed from Kramers-Kroïig relations. The resulting real and imaginary parts of the refractive index (n and k, respectively) are plotted in Figure S8b. We note that the results of the differential fitting procedure reported in the main text and in Sec. S8 are robust if small changes of the equilibrium dielectric function are introduced.

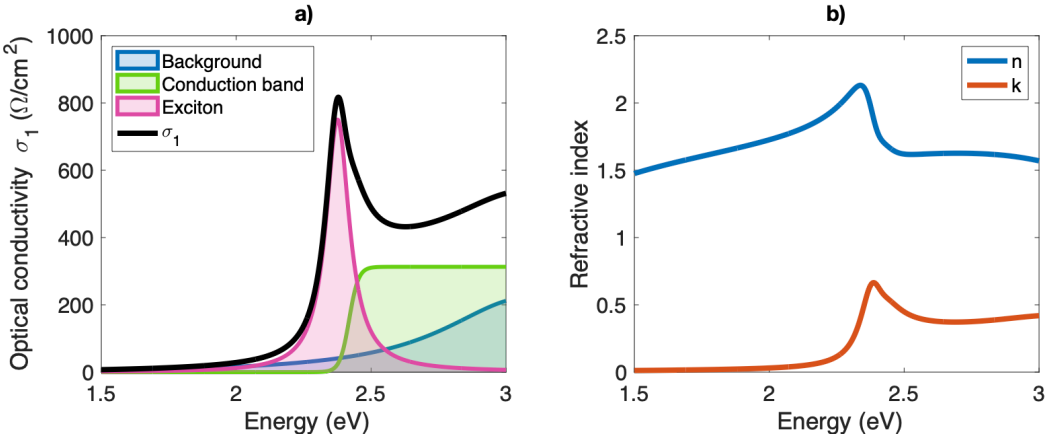

FIG. S8: a) Parametrized real part of the optical conductivity at low temperature (black line). Filled areas represent the different components included in σ_1. b) Real (n) and imaginary (k) parts of the parameterized low temperature refractive index.

S7. EXCITON DENSITY

In order to estimate the number of excitons generated by the pump pulse in each individual nanocube, we start from the equilibrium optical properties of $CsPbBr_3$ (Figure S8) at the pump photon energy and calculate the reflectivity R, which results being $\approx 12\%$. Since the penetration depth is much smaller than the sample thickess, we assume that all the radiation that is not reflected is absorbed. The number of absorbed photons per unit area is then given by

$$N_{\gamma/area} = \frac{F}{\hbar\omega}(1-R) \tag{S4}$$

where $\hbar\omega$ is the photon energy and F is the incident fluence. The incident photons are absorbed within a thickness of 135 nm, which corresponds to the penetration depth l_p at the pump photon energy. The number of absorbed photons per unit volume is then estimated from

$$N_{\gamma/volume} = \frac{N_{\gamma/area}}{l_p}. \tag{S5}$$

Lastly, the number of absorbed photons per nanocube can be obtained by taking into account the volume of each NC, modelled as a cube of $L = 8$ nm side:

$$N_{\gamma/NC} = N_{\gamma/volume} L^3. \tag{S6}$$

We now assume that each absorbed photon produces an electronic excitation, of which 75% are electron-hole bound states and 25% are free carriers. These values are estimated from the contributions of exciton and band edge to the equilibrium optical conductivity at 17 K. Given the values of pump fluence employed in our experiment, we estimate to generate a number of excitons in each NC that can range between 0 and 25. Taking into account that the number of perovskite unit cells within each NC is L^3/a^3, $a = 5.83$ Å, this excitation regime corresponds to a photodoping level up to $\sim 1\%$.

S8. FIT OF PUMP-PROBE DATA

For each measured pump-probe time delay Δt between 4 ps and 130 ps, the spectrally resolved reflectivity variation $\Delta R/R$ is fitted with a function

$$\frac{\Delta R}{R} = \frac{R_{outeq} - R_{eq}}{R_{eq}} \tag{S7}$$

where R_{eq} is the equilibrium reflectivity estimated as $((1-n)^2+k^2)/((1+n)^2+k^2)$, n and k being the real and imaginary parts of the refractive index plotted in Figure S8b. R_{eq} is evaluated as the normal incidence bulk reflectivity because the light penetration depth in the photon energy range of interest is $\lesssim 1$ µm, which is smaller than the film overall thickness (on the order of ~ 10 µm). R_{outeq} is the out-of-equilibrium reflectivity, computed with the same procedure employed for R_{eq} and containing the fit parameters. The free parameters for the differential fit are the out-of-equilibrium free-carriers edge energy position, the sigmoid edge width, the exciton energy and the exciton spectral weight, which represents the smallest subset of free parameters necessary to reproduce the out of equilibrium reflectivity at all fluences and all timescales. The data collected from NC superlattices require to include in the out-of-equilibrium optical conductivity also an additional feature at energy ~2.36 eV, which is smaller then the exciton resonance. Since, at long time delays ($\Delta t \gtrsim 50$ ps), the pump-probe map in Figure 2b shows two distinct peaks between 2.30 eV and 2.37 eV, the experimental data is best described by modelling the new feature below band gap as a sum of two Drude-Lorentz oscillators centered at slightly different energies. This double-peak behaviour likely originates from local inhomogeneities of the samples within the photo-excited area, where superlattices of different lateral size or assembled from NCs of different size can be present and contribute to the measured signal. Figure S9a and b show the the best differential fit at short (5 ps) and long (89 ps) time delays respectively, as reference examples. Fig. S9c and d report the various components of the corresponding out-of-equilibrium optical conductivity (solid lines) obtained from the best fit to the data.

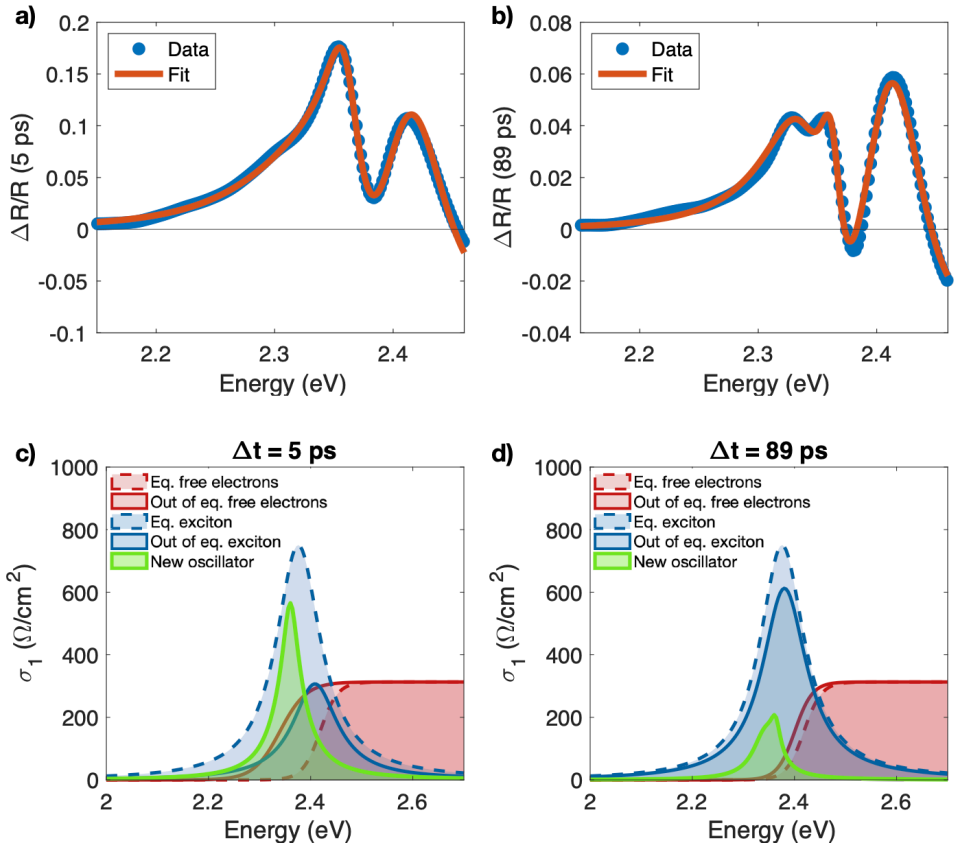

FIG. S9: Differential fit of $\Delta R/R$ data measured on NCs superlattices at 17 K with 230 µJ/cm^2 excitation fluence. a) and b) show the fitted spectra at 5 ps and 89 ps respectively. c) and d) report the equilibrium (dashed lines) and out of equilibrium (solid lines) components of the optical conductivity.

The output parameters of the fit performed at all time delays are displayed in Figure S10, where the blue solid lines represent the values at equilibrium and the red markers are the out-of-equilibrium values extracted from the fit. The top row reports the free-carriers sigmoid edge parameters: the edge amplitude (Fig. S10a) is kept constants at all Δt; the red-shift (Fig. S10b) observed after pump excitation decays with two distinct dynamics, a fast one ($\sim$ 20 ps) and a lower one taking place over hundreds of ps timescale; the edge width displays a broadening in the first $\sim$ 30 ps. Interestingly, this kind of response for the position of the conduction band edge, surviving on a $\sim$ 100 ps timescale, is remarkably different from what usually reported for above-resonance excitation experiments in similar materials, where the large number of free carriers injected in the conduction band leads to a very fast band-gap renormalization followed by a band filling effect after $\sim$ 1 ps [17–19]. The second row in Fig. S10 shows the dynamics of the parameters of the Drude-Lorentz oscillator relative to the excitonic line, namely the exciton energy (Fig. S10d), the plasma frequency ω_p (Fig. S10e) and the exciton width (Fig. S10f). The exciton width does not show significant changes during the relaxation dynamics and is therefore kept constant at all Δt to increase the stability of the fitting procedure. The two bottom rows in Figure S10 report the parameters relative to the Drude-Lorentz oscillators appearing out of equilibrium and associated to the emergence of the cooperative behaviour discussed in the main text. Whereas one single new oscillator is needed to qualitatively reproduce the spectral feature around 2.36 eV at short time delays, two distinct oscillators allow to fit the more structured response observed at long time delays. For consistency, we employed the same model with two new oscillators also at short time delays, where the effect of two distinguished components is covered by the free-carriers edge shift and therefore the error-bars of the associated parameters are larger.

It is relevant to point out that the details of the model employed to fit the $\Delta R/R$ have only a marginal effect on the overall result of the fitting procedure. In addition to what presented in Figure S10, we tested out other models that involved either only one new oscillator, no free-carriers edge width variation, a narrower edge width at equilibrium, or different starting points for the parameters in figures S10g-l. Whatever the fit function employed, the extracted parameters and their relative dynamics display always compatible values and similar trends: the red-shift of the free-carriers edge decaying with two distinct dynamics, the blue-shift and the quench of the exciton recovering to the equilibrium values over $\sim$100 ps and the appearance of new oscillators that are red-shifted and narrower than the equilibrium excitonic peak.

Starting from the differential fit model, we can calculate the total spectral weight

$$SW_{tot} = \int_0^{+\infty} \sigma_{1,tot}(\omega) d\omega \tag{S8}$$

which is, by definition, a conserved quantity depending on the total number of electrons in the system [20]. In particular, we obtain from the data the different contributions:

$$SW_{tot} = SW_{2.36eV} + SW_{exc} + SW_{free} \tag{S9}$$

where $SW_{2.36eV}$ is the spectral weight of the photo-induced cooperative peak at 2.36 eV, SW_{exc} is the spectral weight of the excitonic peak already present in the equilibrium optical conductivity, and SW_{free} is the spectral weight associated to the direct across-gap transitions. Inspection of the spectral weight transfer between the exciton resonance and the free-carrier band is then performed by computing the spectral weight variation ΔSW, compared to equilibrium, of the different components coming into play. Figure S11 reports ΔSW of each component, estimated as the integral of the optical conductivity σ_1 over the energy axis. We observe that the SW lost after photo-excitation by the exciton peak is re-distributed between the new oscillators and free-carrier states in conduction band. At $\Delta t = 5$ ps, for example, the photo-induced decrease of the excitonic spectral weight ($\Delta SW_{exc} \simeq$ -74 ΩeV/cm^2) is perfectly compensated by both the new peak at 2.36 eV ($\Delta SW_{2.36eV} \simeq$ 49 ΩeV/cm^2) and by an increase of in-gap free electron states ($\Delta SW_{free} \simeq$ 25 ΩeV/cm^2). Overall, the spectral weight is conserved at all time delays, as shown by the black markers in Figure S11 representing the sum of all SW variation contributions, which is compatible with zero at all time delays.

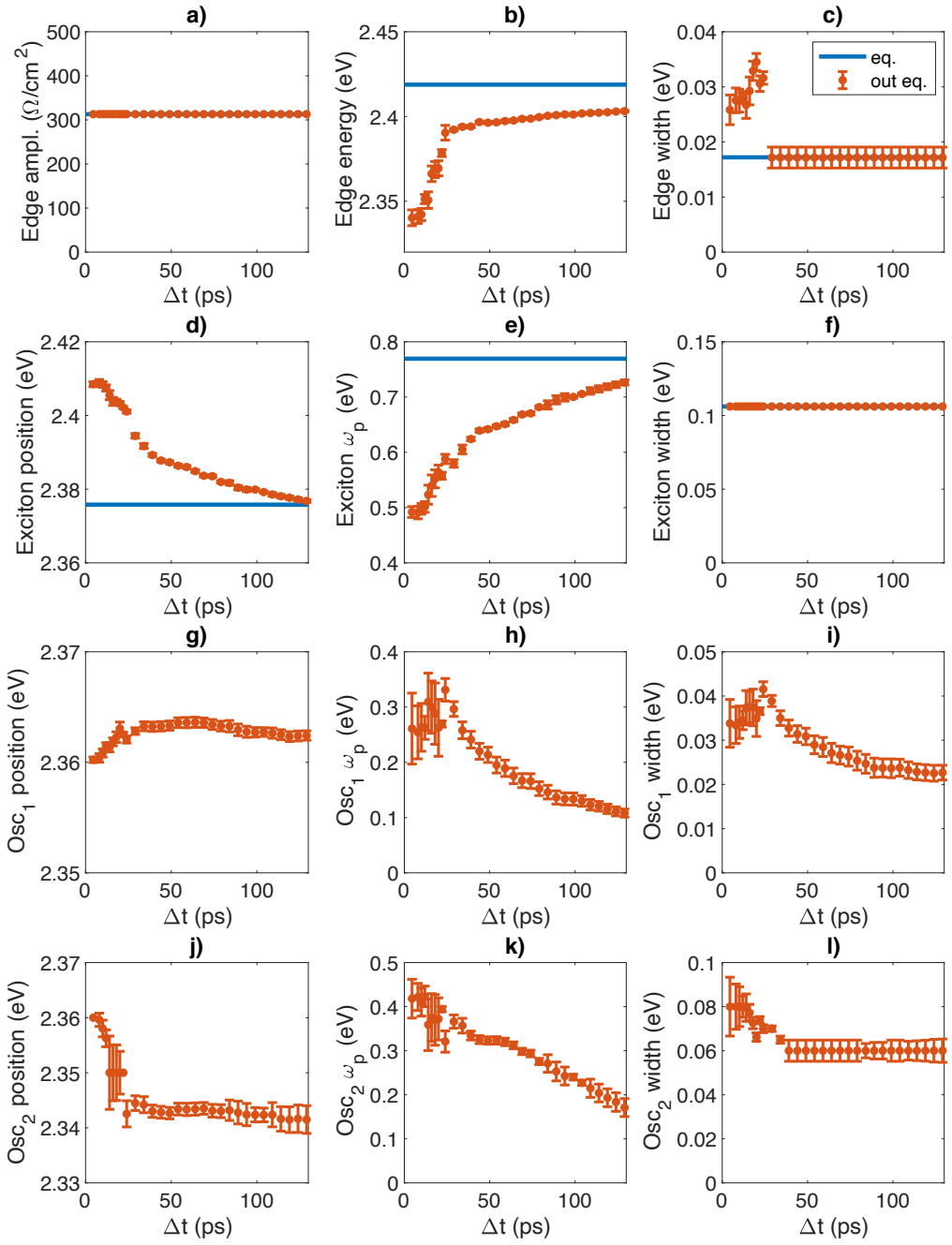

FIG. S10: $\Delta R/R$ fit output parameters for the superlattice NCs sample at 230 µJ/cm^2 excitation fluence. a), b) and c) are the free-carriers edge amplitude, center energy and width, respectively. d), e) and f) represent the exciton parameters: exciton energy, plasma frequency and width, respectively. g)-l) display the Drude-Lorentz model parameters for the new oscillators.

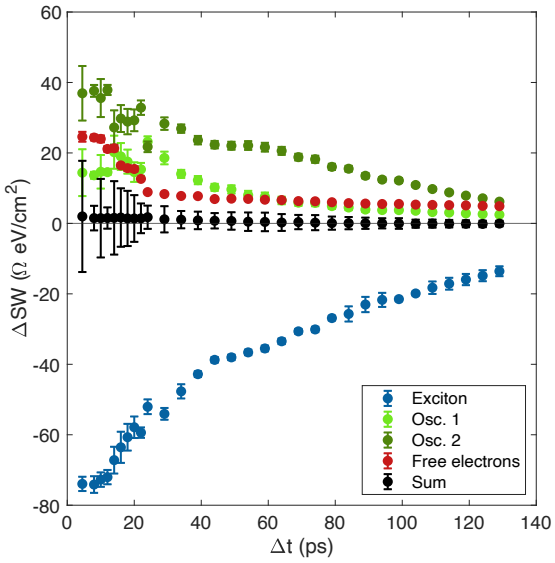

FIG. S11: Spectral weight variation of the exciton (blue), new oscillators (green), and conduction band (red) after pump excitation. Black points represent the sum of the four contributions, indicating SW conservation.

The same fitting procedure is applied to the data collected on the same superlattice sample with lower excitation fluence (30 µJ/cm^2), plotted in Figure S12. The fit results are displayed in Figure S13 for two time delays (5 ps and 89 ps) and in Figure S14 (fit output parameters for all time delays). In this lower fluence excitation scheme the free-electron states edge red-shift is smaller and relaxes with a slow dynamics of 130 ps decay time. The exciton does not show any energy shift, but its spectral weight decreases and is transferred to new oscillators appearing out of equilibrium. Since the free-electrons edge amplitude and width as well as the exciton position and width do not show any significant variation during the relaxation dynamics, they are kept fixed to increase the fit stability.

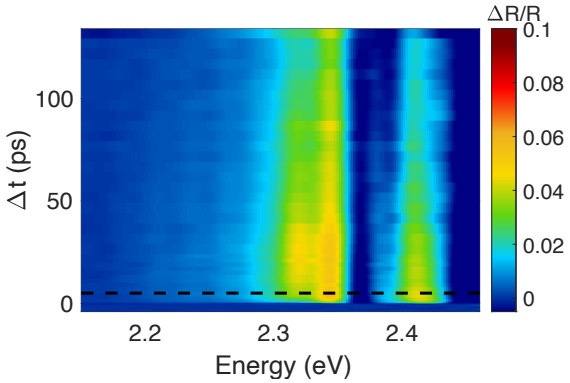

FIG. S12: Ultrafast transient reflectivity of $CsPbBr_3$ superlattice sample measured at 17 K and low excitation fluence (30 µJ/cm^2).

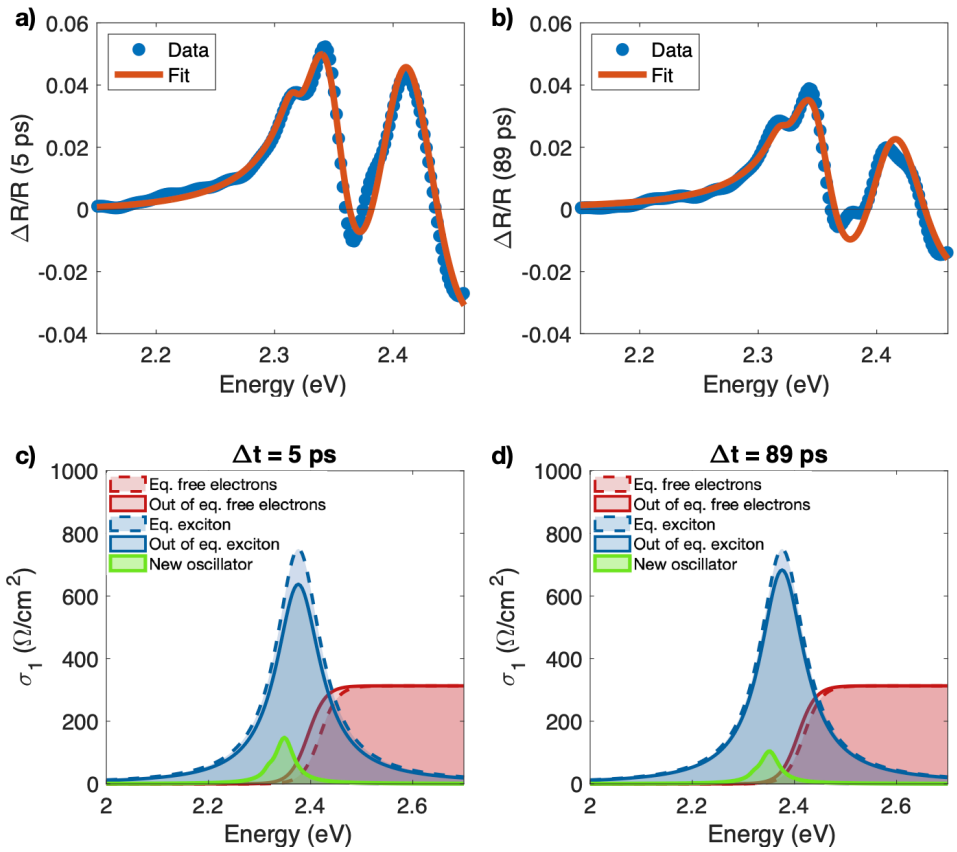

FIG. S13: Differential fit of $\Delta R/R$ data measured on NCs superlattices at 17 K with 30 µJ/cm^2 excitation fluence. a) and b) show the fitted spectra at 5 ps and 89 ps respectively. c) and d) report the equilibrium (dashed lines) and out of equilibrium (solid lines) components of the optical conductivity.

For the disordered NCs sample ($\Delta R/R$ data in Fig. 2), the fit output is reported in figures S15 and S16. In this case, no additional oscillator is needed to reproduce the out of equilibrium optical conductivity. After pump excitation, a red-shift of the free-carriers edge decaying over a $\sim$ 20 ps timescale is revealed, along with a broadening of the edge width and a decrease of the exciton spectral weight. No significant variation of the free-electrons edge amplitude and of the exciton position and width is observed.

We note that, although the dynamics in disordered NC is qualitatively very similar to what observed in ordered samples at high fluence, the measured signal is significantly smaller. This observation suggests that, although the Mott transition takes place in both ordered and disordered NCs, finite size effects [21], which go beyond the scope of this work, emerge when NC are arranged in a disconnected and random network (disordered NCs) thus suppressing coherent hopping and inter-cube delocalization [22].

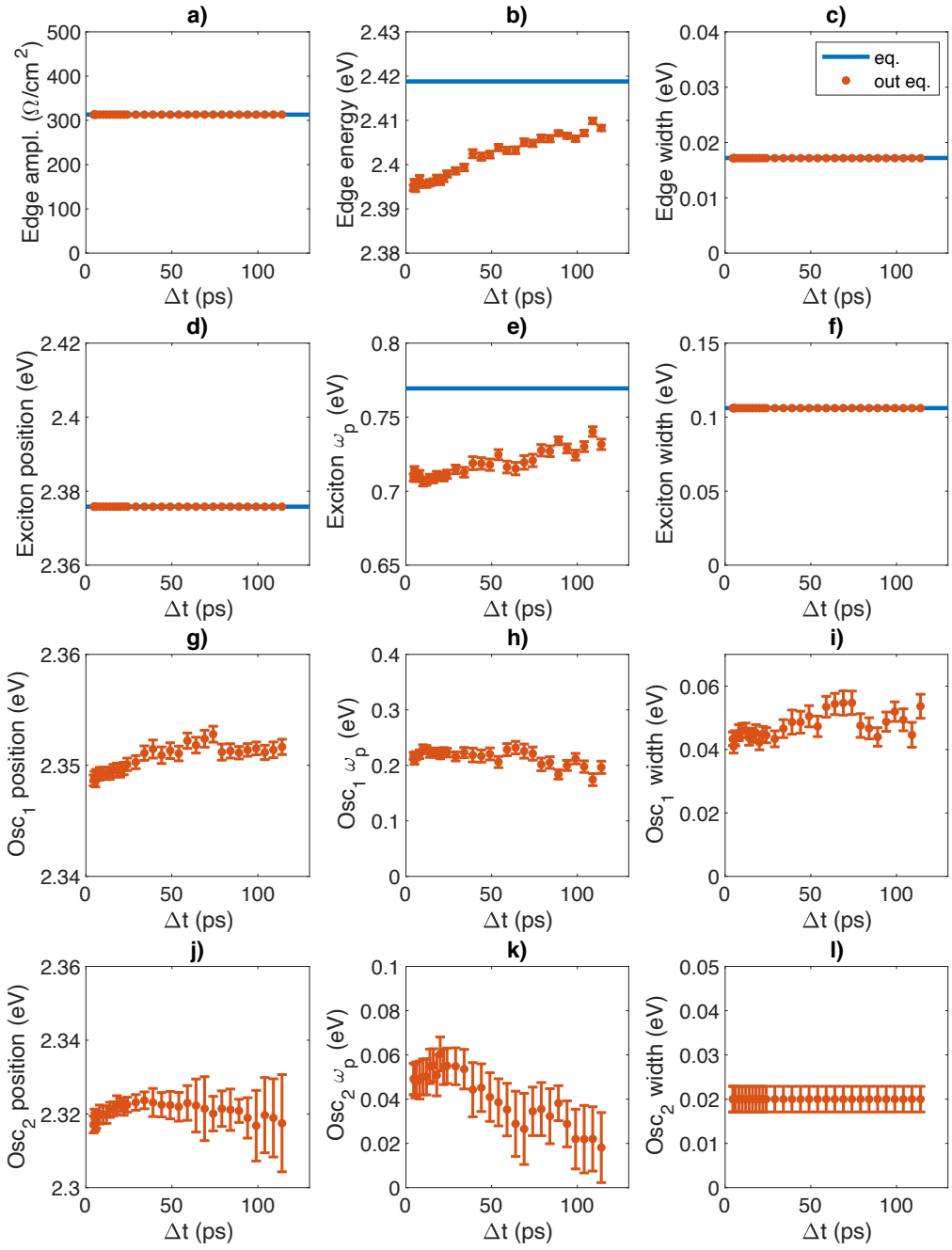

FIG. S14: $\Delta R/R$ fit output parameters for the superlattice NCs sample at 30 µJ/cm^2 excitation fluence. a), b) and c) are the free-carriers edge amplitude, center energy and width, respectively. d), e) and f) represent the exciton parameters: exciton energy, plasma frequency and width, respectively. g)-l) display the Drude-Lorentz model parameters for the new oscillators.

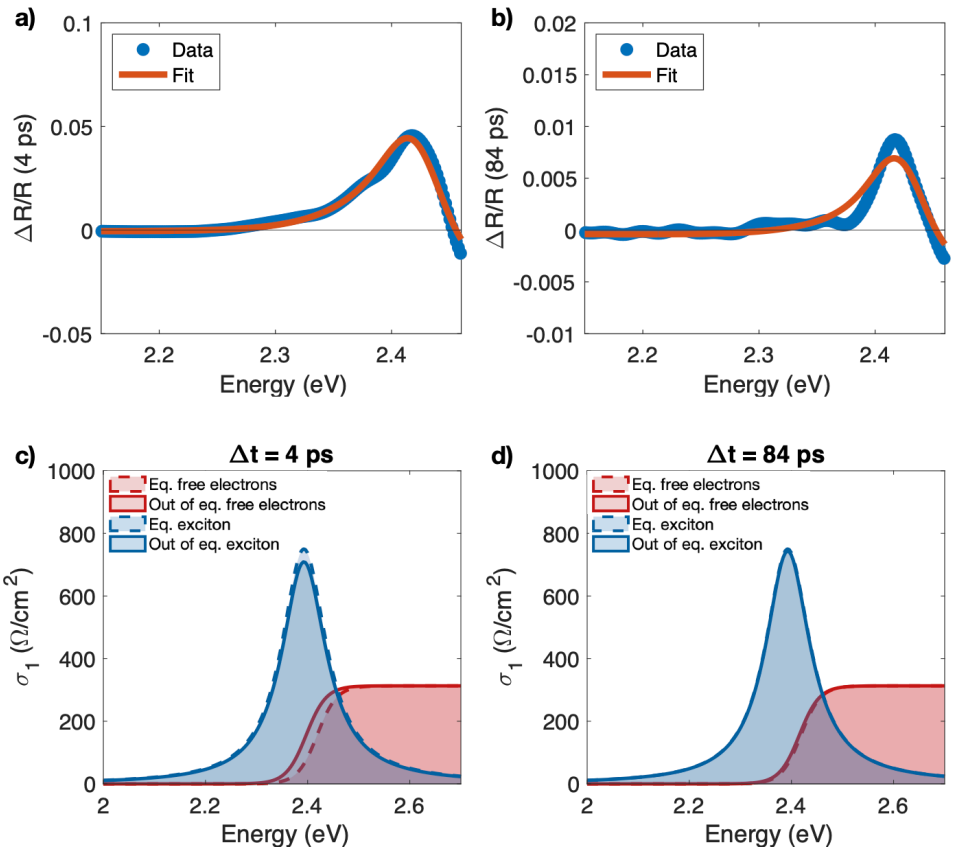

FIG. S15: Differential fit of $\Delta R/R$ data measured on disordered NCs at 17 K. a) and b) show the fitted spectra at 4 ps and 84 ps respectively. c) and d) report the equilibrium (dashed lines) and out of equilibrium (solid lines) components of the optical conductivity.

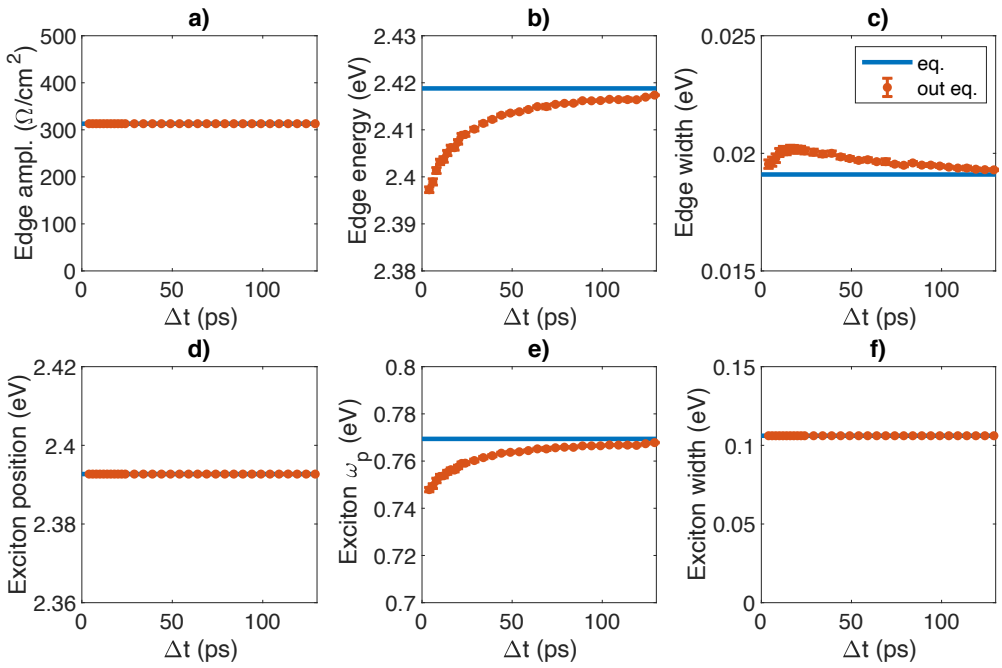

FIG. S16: $\Delta R/R$ fit output parameters for the disordered NCs sample. a), b) and c) are the free-carriers edge amplitude, center energy and width, respectively. d), e) and f) represent the exciton parameters: exciton energy, plasma frequency and width, respectively.

S9. EXPERIMENTAL EVIDENCES OF COOPERATIVE EFFECTS

As introduced in Sec. III, the dipole-dipole long-range interactions among excitons occupying different NCs, as described by $\hat{H}_{int}$, can lead, under proper density conditions, to the formation of a collective superradiant state. This state is generally characterized by a novel red-shifted emission line that scales superlinearly with the excitation fluence [23–26]. In the following, we will report evidence of superradiance in the transient optical spectra obtained by broadband time-resolved reflectivity measurements.

Figure S17a reports the details of the photo-induced changes in the excitonic resonance observed for NC superlattices at 5 ps delay time. The grey and black lines represent the exciton contribution to the equilibrium and out-of-equilibrium optical conductivity, respectively, as obtained from the fit procedure described above (Sec. S8). After the interaction with the excitation light pulse, we observe a $\simeq$60% spectral weight decrease of the excitonic peak, whose out-of-equilibrium optical conductivity is shown by the blue filled area in Fig. S17a, along with the appearance of a new resonance, represented by the green area and highlighted by the black arrow. The linewidth of the new peak is $\simeq$ 40 meV, to be compared to 100 meV width of the main excitonic line. The red-shift δ of this second component with respect to the instantaneous position of the main excitonic resonance is estimated to lay between 40 and 80 meV. The estimated δ allows us to exclude multi-excitons effects, which would cause smaller (10-30 meV) red-shifts in similar systems, [17, 27–29] and would appear also in disordered NCs. Sample to sample variability manifests also in the fine structure of the $\Delta R/R$ signal for $\hbar\omega < 2.37$ eV. As discussed in Section S5, in some samples two distinguished structures (e.g. see data in Fig. 2b at long Δt) are visible particularly for long delays. The presence of these multiple fine structures, which share the same origin and characteristics, is related to local inhomogeneity in the NCs and superlattice sizes. Samples of various aging have been measured and always show a similar response, with variability smaller than that observed from different points on the same sample.

The narrow additional peak emerging in the transient reflectivity properties is visible for both high excitation fluence (230 µJ/cm^2, Figure 2b,d) and low pump intensity (see Fig. S12 corresponding to 30 µJ/cm^2 pump fluence). In order to unambiguously address the cooperative origin of this emergent spectral feature, we performed a detailed fluence dependence study. In Figure S17b we plot the $\Delta R/R$ signal at a fixed time delay (50 ps) as a function of the excitation intensity and integrated over selected spectral regions of interest, which are highlighted by the filled areas in the inset. The top x-axis in Figure S17b reports the excitation intensity expressed as the mean number of excitons in each NC, $\langle N\rangle$ (estimated as described in Section S7). The signal amplitude tends to saturate when $\langle N\rangle \gg 1$, in accordance with what is reported in literature for similar systems [17, 30, 31]. This behavior can be well described, as reported in Ref. 31, by an empirical function of the form $a\langle N\rangle^\alpha/(b+\langle N\rangle^\alpha)$, which accounts for both a low-fluence power-law increase and the high-fluence saturation. If we consider the integrated signal for $\hbar\omega > 2.37$ eV, we obtain $\alpha = (0.91 \pm 0.07)$, whereas for $\hbar\omega < 2.37$ eV we find $\alpha = (1.43 \pm 0.05)$. On disordered NCs (green dots and lines in Fig. S17b), the fluence-dependence of the signal is always linear, independent of the energy region considered.

We note that the fluence-dependent signals shown in Fig. S17b collapse to the same curve above a fluence value of approximately 150-200 µJ/cm^2. This threshold value, which we will indicate as F^t in the following, indicates that the observed cooperative effect is sustained only for moderate densities of excitons. In section V, the discussion on the dynamics of the spectral weight transfer from the exciton to free carrier states allows to set a threshold value for the photonoping n_{eh}, namely n^t_{eh}=0.5% If we calculate the pump fluence necessary to inject this density of photoexcitations, we obtain a threshold fluence $F^t \simeq$190 µJ/cm^2, which is compatible with the fluence at which cooperative effects saturate.

In Figure S17c we report temperature dependent data. The top-right panel shows the transient reflectivity spectra 5 ps after pump excitation at 17 K (blue) and 300 K (red), the latter being multiplied by a normalization factor for comparison purposes. In the main graph we report the $\Delta R/R$ signal at 100 ps, integrated in the 2.15-2.37 eV energy region as a function of temperature T. The comparison to a T^{-1} guide to the eye (gray dashed line in Fig. S17c) indicates a fair agreement with the scaling behavior of the superradiance enhancement factor, that reduces to 1 in the high temperature limit according to a T^{-1} power law [32].

Lastly, we note that, in the same spectral range (2.30-2.37 eV), intense fluorescence induced by the pump beam is observed in the form of stray light emitted by NC superlattices and arriving at the detector. Figure S18 displays the spectrum of the stray light coming at the detector when the pump pulse only impinges onto the sample. The narrow high energy component is associated to the scattering of the pump beam (blue region in Fig. S9). The radiation detected in the spectral range between 2.30 eV and 2.38 eV (orange region in Fig. S9) comes from the $CsPbBr_3$ superlattice sample and is associated to fluorescence emission. This fluorescence is suppressed by $\sim$70% in the disordered NCs, thus further demonstrating that the superlattice is

the key element for achieving the collective superradiant regime described by the inter-unit cell hamiltonian $\hat{H}_{int}$.

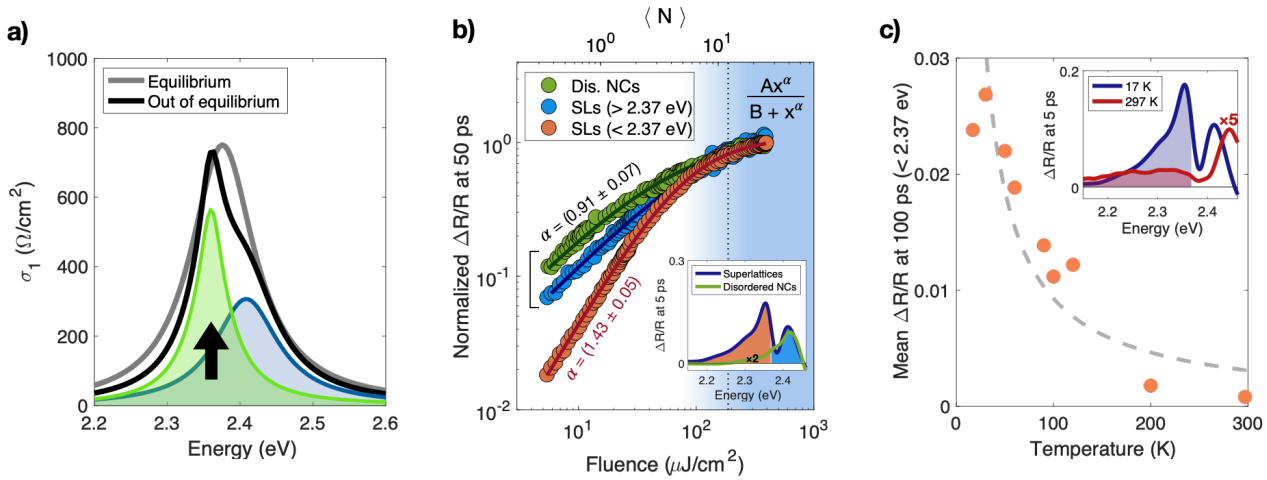

FIG. S17: a) Equilibrium (gray line) and out of equilibrium (black line) excitonic resonance in $CsPbBr_3$ superlattices obtained from differential fit of pump-probe signal at 5 ps delay time. After pump excitation two components are distinguished: the main perovskite exciton (blue area), which undergoes a pronounced decrease of spectral weight, and the additional oscillator (green area) associated to cooperative photo-induced effects. b) Normalized amplitude of $\Delta R/R$ signal at 50 ps delay time as a function of excitation intensity, represented by pump fluence on the bottom axis and mean number of excitons per NC, $\langle N \rangle$, on the top axis. For NC superlattice samples (SLs in legend), the data are collected by integrating the signal in the spectral region below and above 2.37 eV, as highlighted by the coloured areas in the inset (orange and blue respectively). In the top right corner we display the fitting function, where x represents both fluence and $\langle N \rangle$. The dotted vertical line represents the excitation density threshold for the Mott transition, as determined from the temporal dynamics discussed in Sec. V. c) Temperature dependence of $\Delta R/R$ at 100 ps delay time, integrated in the spectral region highlighted in the inset ($\hbar\omega < 2.37$ eV). Dashed gray line: guide to the eye showing the typical T^{-1} dependence of coherence phenomena.

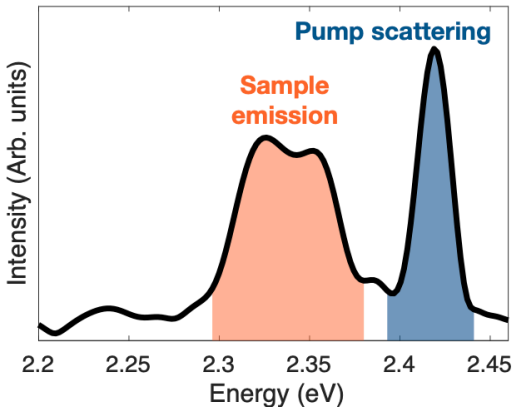

FIG. S18: Spectrum of the stray light detected when the sample is illuminated by the pump beam only.

[1] D. Guerci, M. Capone, and M. Fabrizio, Exciton Mott transition revisited, Physical Review Materials **3**, 054605 (2019).

[2] D. Baranov, S. Toso, M. Imran, and L. Manna, Investigation into the photoluminescence red shift in cesium lead bromide nanocrystal superlattices, The Journal of Physical Chemistry Letters **10**, 655 (2019).

[3] S. Toso, D. Baranov, C. Giannini, S. Marras, and L. Manna, Wide-angle X-ray diffraction evidence of structural coherence in $CsPbBr_3$ nanocrystal superlattices, ACS Materials Letters **1**, 272 (2019).

[4] J. De Roo, M. Ibáñez, P. Geiregat, G. Nedelcu, W. Walravens, J. Maes, J. C. Martins, I. Van Driessche, M. V. Kovalenko, and Z. Hens, Highly dynamic ligand binding and light absorption coefficient of cesium lead bromide perovskite nanocrystals, ACS Nano **10**, 2071 (2016).

[5] M. V. Kovalenko and M. I. Bodnarchuk, Lead halide perovskite nanocrystals: From discovery to self-assembly and applications, Chimia **71**, 461 (2017).

[6] Y. Nagaoka, K. Hills-Kimball, R. Tan, R. Li, Z. Wang, and O. Chen, Nanocube superlattices of cesium lead bromide perovskites and pressure-induced phase transformations at atomic and mesoscale levels, Advanced Materials **29**, 1606666 (2017).

[7] J. S. van der Burgt, J. J. Geuchies, B. van der Meer, H. Vanrompay, D. Zanaga, Y. Zhang, W. Albrecht, A. V. Petukhov, L. Filion, S. Bals, et al., Cuboidal supraparticles self-assembled from cubic $CsPbBr_3$ perovskite nanocrystals, The Journal of Physical Chemistry C **122**, 15706 (2018).

[8] Y. Tong, E.-P. Yao, A. Manzi, E. Bladt, K. Wang, M. Döblinger, S. Bals, P. Müller-Buschbaum, A. S. Urban, L. Polavarapu, et al., Spontaneous self-assembly of perovskite nanocrystals into electronically coupled supercrystals: toward filling the green gap, Advanced Materials **30**, 1801117 (2018).

[9] C. A. López, C. Abia, M. C. Alvarez-Galván, B.-K. Hong, M. V. Martínez-Huerta, F. Serrano-Sánchez, F. Carrascoso, A. Castellanos-Gómez, M. T. Fernández-Díaz, and J. A. Alonso, Crystal structure features of $CsPbBr_3$ perovskite prepared by mechanochemical synthesis, ACS Omega **5**, 5931 (2020).

[10] S. Toso, D. Baranov, D. Altamura, F. Scattarella, J. Dahl, X. Wang, S. Marras, A. P. Alivisatos, A. Singer, C. Giannini, et al., Multilayer diffraction reveals that colloidal superlattices approach the structural perfection of single crystals, ACS Nano **15**, 6243 (2021).

[11] D. Baranov, A. Fieramosca, R. X. Yang, L. Polimeno, G. Lerario, S. Toso, C. Giansante, M. D. Giorgi, L. Z. Tan, D. Sanvitto, et al., Aging of self-assembled lead halide perovskite nanocrystal superlattices: Effects on photoluminescence and energy transfer, ACS Nano **15**, 650 (2020).

[12] F. Preda, V. Kumar, F. Crisafi, D. G. F. Del Valle, G. Cerullo, and D. Polli, Broadband pump-probe spectroscopy at 20-mhz modulation frequency, Optics Letters **41**, 2970 (2016).

[13] Y. Guo, O. Yaffe, T. D. Hull, J. S. Owen, D. R. Reichman, and L. E. Brus, Dynamic emission stokes shift and liquid-like dielectric solvation of band edge carriers in lead-halide perovskites, Nature communications **10**, 1 (2019).

[14] W. Shcherbakov-Wu, P. C. Sercel, F. Krieg, M. V. Kovalenko, and W. A. Tisdale, Temperature-independent dielectric constant in $CsPbBr_3$ nanocrystals revealed by linear absorption spectroscopy, The Journal of Physical Chemistry Letters **12**, 8088 (2021).

[15] L. Protesescu, S. Yakunin, M. I. Bodnarchuk, F. Krieg, R. Caputo, C. H. Hendon, R. X. Yang, A. Walsh, and M. V. Kovalenko, Nanocrystals of cesium lead halide perovskites ($CsPbX_3$, X= Cl, Br, and I): novel optoelectronic materials showing bright emission with wide color gamut, Nano Letters **15**, 3692 (2015).

[16] J. Li, X. Yuan, P. Jing, J. Li, M. Wei, J. Hua, J. Zhao, and L. Tian, Temperature-dependent photoluminescence of inorganic perovskite nanocrystal films, RSC advances **6**, 78311 (2016).

[17] J. Aneesh, A. Swarnkar, V. Kumar Ravi, R. Sharma, A. Nag, and K. Adarsh, Ultrafast exciton dynamics in colloidal $CsPbBr_3$ perovskite nanocrystals: Biexciton effect and auger recombination, The Journal of Physical Chemistry C **121**, 4734 (2017).

[18] P. Franceschini, L. Carletti, A. P. Pushkarev, F. Preda, A. Perri, A. Tognazzi, A. Ronchi, G. Ferrini, S. Pagliara, F. Banfi, et al., Tuning the ultrafast response of Fano resonances in halide perovskite nanoparticles, ACS Nano **14**, 13602 (2020).

[19] M. B. Price, J. Butkus, T. C. Jellicoe, A. Sadhanala, A. Briane, J. E. Halpert, K. Broch, J. M. Hodgkiss, R. H. Friend, and F. Deschler, Hot-carrier cooling and photoinduced refractive index changes in organic–inorganic lead halide perovskites, Nature Communications **6**, 1 (2015).

[20] F. Wooten, Optical Properties of Solids (Academic Press, 1972).

[21] J. X. Wang and S. Kais, Finite-size scaling for Mott metal-insulator transition on a half filled nonpartite lattice, Phys. Rev. B **66**, 081101 (2002).

[22] D. D. Blach, V. A. Lumsargis, D. E. Clark, C. Chuang, K. Wang, L. Dou, R. D. Schaller, J. Cao, C. W. Li, and L. Huang, Superradiance and Exciton Delocalization in Perovskite Quantum Dot Superlattices, Nano Letters **22**, 7811 (2022).

[23] G. Rainò, M. A. Becker, M. I. Bodnarchuk, R. F. Mahrt, M. V. Kovalenko, and T. Stöferle, Superfluorescence from lead halide perovskite quantum dot superlattices, Nature **563**, 671 (2018).

[24] G. Findik, M. Biliroglu, D. Seyitliyev, J. Mendes, A. Barrette, H. Ardekani, L. Lei, Q. Dong, F. So, and K. Gundogdu, High-temperature superfluorescence in methyl ammonium lead iodide, Nature Photonics **15**, 676 (2021).

[25] F. Krieg, P. C. Sercel, M. Burian, H. Andrusiv, M. I. Bodnarchuk, T. Stöferle, R. F. Mahrt, D. Naumenko, H. Amenitsch, G. Rainò, and M. V. Kovalenko, Monodisperse long-chain sulfobetaine-capped $CsPbBr_3$ nanocrystals and their superfluorescent assemblies, ACS Central Science **7**, 135 (2020).

[26] I. Cherniukh, G. Rainò, T. Stöferle, M. Burian, A. Travesset, D. Naumenko, H. Amenitsch, R. Erni, R. F. Mahrt, M. I. Bodnarchuk, and M. V. Kovalenko, Perovskite-type superlattices from lead halide perovskite nanocubes, Nature **593**, 535 (2021).

[27] G. Rainò, G. Nedelcu, L. Protesescu, M. I. Bodnarchuk, M. V. Kovalenko, R. F. Mahrt, and T. Stöferle, Single cesium lead halide perovskite nanocrystals at low temperature: fast single-photon emission, reduced blinking, and exciton fine structure, ACS Nano **10**, 2485 (2016).

[28] M. Fu, P. Tamarat, H. Huang, J. Even, A. L. Rogach, and B. Lounis, Neutral and charged exciton fine structure in single lead halide perovskite nanocrystals revealed by magneto-optical spectroscopy, Nano Letters **17**, 2895 (2017).

[29] Y. Tang, D. Poonia, M. Van Der Laan, D. Timmerman, S. Kinge, L. D. Siebbeles, and P. Schall, Electronic coupling of highly ordered perovskite nanocrystals in supercrystals, ACS Applied Energy Materials **5**, 5415 (2022).

[30] M. Gramlich, B. J. Bohn, Y. Tong, L. Polavarapu, J. Feldmann, and A. S. Urban, Thickness-dependence of exciton–exciton annihilation in halide perovskite nanoplatelets, The Journal of Physical Chemistry Letters **11**, 5361 (2020).

[31] V. I. Klimov, Optical nonlinearities and ultrafast carrier dynamics in semiconductor nanocrystals, The Journal of Physical Chemistry B **104**, 6112 (2000).

[32] F. Mattiotti, M. Kuno, F. Borgonovi, B. Jankó, and G. L. Celardo, Thermal decoherence of superradiance in lead halide perovskite nanocrystal superlattices, Nano Letters **20**, 7382 (2020).